


 Cite this: *RSC Adv.*, 2024, 14, 14868

 Received 22nd February 2024
 Accepted 29th April 2024

DOI: 10.1039/d4ra01372g

rsc.li/rsc-advances

Synergistic effect between In_2O_3 and ZrO_2 in the reverse water gas shift reaction†

 Jiayu Dong,^a Hong Wang,^d Guofeng Zhao,^{id}*^c Dong Jiang^{*b} and Haitao Xu^{id}*^a

Efficient activation of CO_2 at low temperature was achieved through the interface effect between In_2O_3 and ZrO_2 by their geometric and electronic effects. The results show that $75\text{In}_2\text{O}_3\text{-}25\text{ZrO}_2$ (In_2O_3 : ZrO_2 molar ratio of 3 : 1), as a catalyst for the reverse water gas shift reaction, can achieve 28% CO_2 conversion with 96% CO selectivity at 400 °C, 0.1 MPa, a H_2 : CO_2 molar ratio of 3 : 1 and a gas hourly space velocity of 10 000 $\text{mL g}^{-1} \text{h}^{-1}$. *In situ* FTIR experiments provide a basis for clarifying the pivotal role of formate (facilitated at $\text{In}_2\text{O}_3\text{-ZrO}_2$ interface) in this reaction.

1. Introduction

Throughout the course of industrial development, humans have heavily relied on fossil fuels to meet the substantial demand for energy, resulting in a continuous increase in greenhouse gas emissions and exacerbation of climate change.¹ Utilizing carbon dioxide, an abundant and economical carbon resource, to produce high-value-added chemicals or liquid fuels is of significant importance for energy conservation, emissions reduction, and the sustainable utilization of carbon resources.² In recent years, carbon capture and utilization (CCU) technology has attracted much attention and is considered as one of the useable ways to reduce CO_2 emissions.^{3–7} The thermal catalytic reduction of CO_2 refers to the process of converting CO_2 into hydrocarbons or carbon monoxide (CO) with green hydrogen, typically carried out with the aid of catalysts at elevated temperature.⁸ The rapid development of renewable energy lowers the cost of green hydrogen production,⁹ prompting the urgent need for catalysts with high activity, selectivity, and stability.

The reverse water gas shift (RWGS) reaction hydrogenates CO_2 into CO, which can be further used to synthesize methanol, breaking through the thermodynamic equilibrium limit of direct methanol production from CO_2 ,^{10,11} and can also be

combined with Fischer–Tropsch synthesis (FTS) process to prepare useful chemicals such as olefins.^{12–15} Whether producing methanol through the CAMERE method (carbon dioxide hydrogenation to form methanol *via* a RWGS reaction) or preparing low-carbon olefins *via* the CO_2 -FTS method, the RWGS reaction with high CO yield is a crucial step. Therefore, the RWGS reaction is considered as the most promising and prospective pathway in re-utilizing CO_2 .

Catalysts used in the RWGS reaction can be classified into noble metal catalysts, such as Rh,¹⁶ Ru,¹⁷ and Pt,¹⁸ and non-noble metal catalysts, such as Co,¹⁹ Fe,^{20,21} and Mo.^{22,23} The noble metal catalysts exhibit outstanding performance due to their effective hydrogen dissociation capabilities, but their high costs and instability (nanoparticle agglomeration) limit their industrial application; the non-noble metal catalysts need high temperature to deliver the same performance as noble metal ones.²⁴ Therefore, there is of significant importance in developing low-temperature, high-performance catalysts to address these limitations. In recent years, indium oxide (In_2O_3) has been found as a proficient catalyst for CO_2 hydrogenation, with its pronounced catalytic activity attributed to the abundant oxygen vacancy (O_v) on its surface.^{25–28} Furthermore, In_2O_3 can be easily supported and/or modified by promoters to form more O_v sites, thereby activating more CO_2 molecules, and stabilizing surface intermediates near O_v .^{29–33}

Moreover, ZrO_2 is also used as catalyst support in RWGS reaction, but its role plays in the reaction is still unclear.³⁴ Unfortunately, there are relatively few reports related to the synergistic interfacial effect between In_2O_3 and ZrO_2 , hampering the rational design of mixed oxides for the RWGS reaction. For the optimal $75\text{In}_2\text{O}_3\text{-}25\text{ZrO}_2$ (In_2O_3 : ZrO_2 molar ratio of 3 : 1) with abundant $\text{In}_2\text{O}_3\text{-ZrO}_2$ interface, 28% CO_2 conversion and 96% CO selectivity can be achieved at 400 °C, 0.1 MPa, H_2 : CO_2 molar ratio of 3 : 1 and GHSV (gas hourly space velocity) of 10 000 $\text{mL g}^{-1} \text{h}^{-1}$. Control experiments and characterization results testify that the as-formed oxygen

^aSchool of Chemical Engineering, East China University of Science and Technology, Shanghai 200237, China. E-mail: xuhaitao@ecust.edu.cn

^bSchool of Chemistry and Molecular Engineering, East China University of Science and Technology, Shanghai 200237, China. E-mail: jiangdong@ecust.edu.cn

^cKey Laboratory of Functional Molecular Solids, Ministry of Education, College of Chemistry and Materials Science, Anhui Normal University, Wuhu 241002, China. E-mail: gfzhao@chem.enu.edu.cn

^dInstitute of Optical Functional Materials for Biomedical Imaging, School of Chemistry and Pharmaceutical Engineering, Shandong First Medical University, Shandong Academy of Medical Sciences, Taian 271016, China

 † Electronic supplementary information (ESI) available. See DOI: <https://doi.org/10.1039/d4ra01372g>


vacancies (O_{vs}) caused by the reduction of In_2O_3 to In_2O_{3-x} significantly enhance catalytic activity for $75In_2O_3-25ZrO_2$. In addition, *in situ* Fourier transform infrared spectroscopy (FTIR) shows that $HCOO^*$ (formate) plays an important role in this reaction. For $75In_2O_3-25ZrO_2$ with abundant $In_2O_3-ZrO_2$ interface, $HCOO^*$ is easily hydrogenated into CO. However, for In_2O_3 , the content of $HCOO^*$ is relatively lower, thus contributing to its lower catalytic activity. For ZrO_2 , the CO_3^{2-} is relatively stable, correlating well with its low catalytic activity. This work elucidates the synergistic effect between mixed In_2O_3 and ZrO_2 , paving a way to design industrial catalyst with abundant $In_2O_3-ZrO_2$ interface to offer excellent catalytic performance for RWGS reaction.

2. Experimental

2.1. Catalyst preparation

The mixed In-Zr oxides were synthesized by a co-precipitation method. For instance, for the $75In_2O_3-25ZrO_2$ ($In_2O_3:ZrO_2$ molar ratio of 3:1), 1.5612 g $In(NO_3)_3 \cdot xH_2O$ and 0.3713 g $Zr(NO_3)_4 \cdot 5H_2O$ were dissolved in 20 mL deionized water, followed by the addition of the mixed solution of NH_4OH (10 mL, 25 wt% in H_2O , Alfa Aesar) and ethanol (30 mL, Titan) until the pH reaching 9.2. The resulting slurry was heated to 80 °C with vigorous stirring and aged for 30 min. Then the solid was separated by high-pressure filtration, washed with 500 mL deionized water, dried at 60 °C for 12 h, and calcined at 500 °C (heating rate of ca. 2 °C min^{-1}) for 3 h. Other catalysts such as In_2O_3 , ZrO_2 , and $aIn_2O_3-bZrO_2$ (a and b represent In_2O_3 and ZrO_2 molar ratio ($a = 25\%$, 50% , and 75% , $b = 1 - a$)) were prepared using the same method by simply tuning the molar ratio of $In(NO_3)_3 \cdot xH_2O$ and $Zr(NO_3)_4 \cdot 5H_2O$.

2.2. Catalyst characterization

The N_2 sorption was conducted using the ASAP 2020 instrument (Mack, USA). The specific surface area (S_{BET}) was determined by Brunauer-Emmett-Teller (BET) model and the pore size was calculated by Barret-Joyner-Halenda (BJH) model. The In and Zr loadings were detected by an inductively coupled plasma-atomic emission spectrometry (ICP-AES) at 167–785 nm/725 instrument (Agilent Corporation, USA). The power X-ray diffraction (XRD) patterns of catalysts were obtained on a Rigaku D/Max 2550 VB/PC instrument (Rigaku, Japan) using a scanning rate of 10° min^{-1} . The fine structures were observed by a transmission electron microscopy (TEM) at an accelerating voltage of 200 kV on JEM-2100 (JEOL, Japan). The energy dispersive X-ray spectroscopy (EDX) was measured by the JEM-2100 (JEOL, Japan) with an amplification of 8000–300 000. X-ray photoelectron spectroscopy (XPS) was measured at ESCALAB 250Xi photoelectron spectrometer (Thermo Fisher Scientific, USA) equipped with an Al-K α X-ray source. All the binding energies were calibrated on the basis of the internal standard of the binding energy of C 1s (284.8 eV). Electron paramagnetic resonance (EPR) spectroscopy was performed using the CIQTEK EPR200-Plus. Spectra were collected accumulating 1 scan for field sweeps of 3250–3850 G at 298 K with a magnetic field

modulation frequency of 100 kHz. The spectrum of an empty tube was subtracted to correct for the background signal.

The experiments of H_2 -temperature programmed reduction (H_2 -TPR) and CO_2 -temperature programmed desorption (CO_2 -TPD) were carried out on a ChemBET Pulsar automatic adsorption apparatus (Quantachrome Company, USA) equipped with a thermal conductivity detector (TCD), and the efflux were monitored by an on-line mass spectrometer (MS, SHP8400PMS-L, Shanghai Sunny Hengping Scientific Instrument Co. Ltd, China). For H_2 -TPR, each catalyst (0.1 g) was pretreated in Ar flow (30 mL min^{-1}) at 300 °C for 0.5 h and cooled down to room temperature. Then, the gas was switched to H_2/Ar flow (10 vol% H_2 , 50 mL min^{-1}) and the catalyst was reduced from room temperature to 800 °C at a heating rate of 10 °C min^{-1} . For CO_2 -TPD, each catalyst (0.1 g) was pretreated in Ar flow (30 mL min^{-1}) at 400 °C for 1 h, and then reacted in mixture gas (the molar ratio of $H_2:CO_2$ is 3:1, 50 mL min^{-1}) at 400 °C for 2 h. Then, the catalyst was cooled to 50 °C in the same flow followed by CO_2 (50 mL min^{-1}) adsorption at 50 °C for 2 h. After that, the catalyst was flushed in He flow (50 mL min^{-1}) for 0.5 h, followed by heated from 50 to 800 °C at a rate of 10 °C min^{-1} , and signals of CO_2 were monitored by MS on line.

The *in situ* Fourier transform infrared (FT-IR) was conducted on a IRPrestige-21 equipment (Shimadzu, Japan). A resolution of 8 cm^{-1} and scanning times of 50. 50 mg catalyst and 100 mg KBr were pressed into a wafer and placed in the *in situ* chamber. All the samples were pretreated at 400 °C in H_2 flow (37.5 mL min^{-1}) for 10 min and cooled to the room temperature to obtain the background spectrum. When the adsorption of CO_2 , the flow was switched to CO_2 (12.5 mL min^{-1} , 99.99%) at room temperature for 10 min, after that, CO_2 was switched off and the catalyst was maintained at 50 °C for 2 h. Subsequently, catalyst was purged with a He flow (30 mL min^{-1}) for 5 minutes and then raised from 50 to 400 °C, with the spectra were collected. After raising to 400 °C, the flow was switched to H_2 for 10 s, H_2 was switched off and the spectra was collected at 0.5 MPa. When the co-adsorption of CO_2 and H_2 , the flow was switched to the mixed gas (the molar ratio of $H_2:CO_2$ is 3:1, 50 mL min^{-1}). The temperature was raised from 100 to 400 °C and the spectra were collected.

2.3. Catalytic evaluation

In this work, a continuous fixed-bed reactor was used to evaluate the performance of catalysts. Typically, 0.3 g catalyst was loaded into a reactor with an inner diameter of 7 mm and the length of 700 mm. H_2 (36 mL min^{-1}), CO_2 (12 mL min^{-1}), and Ar (2 mL min^{-1}) was controlled by mass flow controllers, forming a $H_2/CO_2/Ar$ (molar ratio of 72/24/4) mixture and passing through the catalyst bed. The Ar was used as the internal standard gas. Then, the temperature was successively raised from room temperature to 400 °C and maintained for 2 h. The effluent was analyzed by online gas chromatography (GC7900), equipped with a thermal conductivity detector (TCD) and TDX-1 column. The CO_2 conversion (X_{CO_2}), CO selectivity (S_{CO}), CO yield (Y_{CO}) and CH_4 selectivity (S_{CH_4}) were calculated as follows:



$$X_{\text{CO}_2} = \frac{\text{CO}_2^{\text{in}} - \text{CO}_2^{\text{out}}}{\text{CO}_2^{\text{in}}} \times 100\% \quad (1)$$

$$S_{\text{CO}} = \frac{\text{CO}^{\text{out}}}{\text{CO}_2^{\text{in}} - \text{CO}_2^{\text{out}}} \times 100\% \quad (2)$$

$$Y_{\text{CO}} = X_{\text{CO}_2} \times S_{\text{CO}} \quad (3)$$

$$S_{\text{CH}_4} = \frac{\text{CH}_4^{\text{out}}}{\text{CO}_2^{\text{in}} - \text{CO}_2^{\text{out}}} \times 100\% \quad (4)$$

CO_2^{in} and CO_2^{out} represent the concentration of CO_2 at the inlet and outlet, respectively; CO^{out} represents the concentration of CO at the outlet; CH_4^{out} represent the concentration of CH₄ at the outlet.

3. Results and discussion

3.1. Structures and chemical states of fresh catalysts

Five In_2O_3 - ZrO_2 catalysts were prepared by the co-precipitation method, varying the molar content of In_2O_3 of 0, 25%, 50%, 75% and 100%. The inductively coupled plasma-atomic emission spectrometry (ICP-OES) measurements confirmed that In and Zr contents were almost identical to the theoretical value. Adding ZrO_2 to In_2O_3 will slightly increase the specific surface area (Table S1[†]), but the specific surface area of $75\text{In}_2\text{O}_3$ - 25ZrO_2 is close to that of In_2O_3 , albeit the catalyst area is not the key factor determining catalytic activity.³⁵ Moreover, the type IV hysteresis loop testifies the mesoporous structure of this series of catalysts (Fig. S1[†]). TEM images of this series of catalysts show the similar morphologies, with the diameter of 8–15 nm (Fig. S2[†]).

For $75\text{In}_2\text{O}_3$ - 25ZrO_2 , the average particle size is 10.0 ± 1.4 nm, and the HRTEM images illustrate the lattice distances of 0.292, 0.275, and 0.297 nm, corresponding to the In_2O_3 (222), In_2O_3 (321), and t - ZrO_2 (101) planes, respectively (Fig. S3a and b[†]). The STEM-EDX mapping images show that In and Zr elements are randomly distributed on the catalyst surface (Fig. S3c and d[†]), forming abundant In_2O_3 - ZrO_2 interface and tentatively contributing to excellent catalytic performance.

X-ray diffraction (XRD) was used to figure out the effect of Zr modification on bulk structure. The XRD patterns in Fig. S4a,[†] display that the pure ZrO_2 (*i.e.*, $0\text{In}_2\text{O}_3$ - 100ZrO_2) prefers to crystallize to its thermodynamically stable monoclinic structure; the presence of In steers the growth of ZrO_2 toward metastable tetragonal phase,²⁸ suggesting that partial In is incorporated into the ZrO_2 lattice in the form of In–O–Zr bond, as evidenced by the HRTEM image of $75\text{In}_2\text{O}_3$ - 25ZrO_2 sample.³⁶ The transition from In–O–In bond to In–O–Zr bond should greatly improve the CO_2 conversion and CO selectivity of In_2O_3 - ZrO_2 catalysts (see the results in Section 3.2). Owing to the fact that the lattice parameters of cubic In_2O_3 (JCPDS card 06-0416) and t - ZrO_2 (JCPDS card 37-1413) are akin, their XRD patterns are virtually identical. However, as shown in Fig. S4b,[†] the diffraction peak moves from 30.167° (t - ZrO_2 (111)) to 30.580° (c - In_2O_3 (222)) with the increase of In_2O_3 content, and such tiny peak shift confirms the generation of In_2O_3 - ZrO_2 solid solution.

The surface chemical states of In_2O_3 - ZrO_2 catalysts were characterized by XPS (Fig. 1) and EPR (Fig. S6[†]). The symmetric binding energy peaks at ~452 and ~444.3 eV testify that In species exists in the form of In^{3+} .³⁷ With the increase of In_2O_3 content, the binding energy of In^{3+} decreases slightly, indicating the electron transfer from Zr to In.³⁶ The symmetric binding energy peaks at ~184.5 and ~182.0 eV testify that Zr species exists in the form of Zr^{4+} .³⁸ For $50\text{In}_2\text{O}_3$ - 50ZrO_2 and $75\text{In}_2\text{O}_3$ - 25ZrO_2 , the binding energies of Zr are higher than that of $25\text{In}_2\text{O}_3$ - 75ZrO_2 , also coinciding with the electron transfer. For the O 1s XPS spectra, the major peak at 529.5–531.0 eV corresponds to lattice oxygen, the peak at 531.0–532.0 eV to O_v , and the one at 532.5–533.0 eV to surface OH.³⁹ Obviously, with the increase of In_2O_3 content, the O_v content increases progressively. Fig. S5[†] shows that there is a positive correlation between the CO STY (space-time yield) and the oxygen vacancy concentration, which means that the O_v may play an important role in the RWGS reaction. Furthermore, the EPR results in Fig. S6[†] reveals a signal of $g = 1.890$ for fresh In_2O_3 , which implies that the surface vacancies exist on In_2O_3 .⁴⁰ Pure ZrO_2 sample exhibits an isotropic EPR signal at $g = 1.973$, which is assigned to the bulk Zr^{3+} ions located at axially symmetric sites. The $75\text{In}_2\text{O}_3$ - 25ZrO_2 demonstrates a prominent signal that can be attributed to unpaired electrons trapped in symmetric site at g

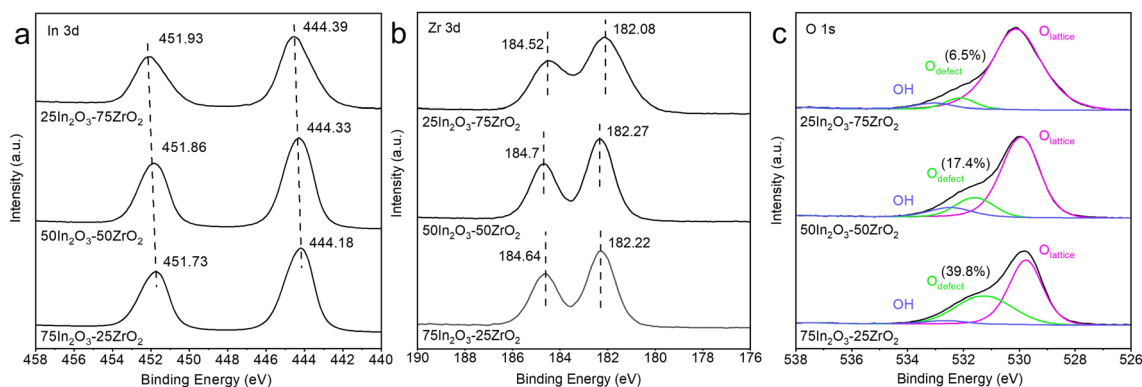


Fig. 1 XPS spectra of (a) In 3d, (b) Zr 3d, and (c) O 1s for the $25\text{In}_2\text{O}_3$ - 75ZrO_2 , $50\text{In}_2\text{O}_3$ - 50ZrO_2 and $75\text{In}_2\text{O}_3$ - 25ZrO_2 catalyst.



= 2.004, which is always typically assigned to oxygen vacancies.⁴¹ This means the synergistic effect between In₂O₃ and ZrO₂ in 75In₂O₃-25ZrO₂ solid solution is beneficial to produce new oxygen vacancies at $g = 2.004$, which is in line with the XPS result.

H₂ temperature-programmed reduction (H₂-TPR) tests were conducted to determine the reactivity of the In₂O₃-ZrO₂ catalyst toward H₂ activation in the temperature range of 50–800 °C, as shown in Fig. S7a.† The H₂-TPR profiles revealed that reduction temperature of bulk In₂O₃ in In₂O₃ and 75In₂O₃-25ZrO₂ are 662 °C and 697 °C respectively, while the reduction temperature of surface In₂O₃ are 189 °C and 225 °C respectively. However, the H₂-TPR of ZrO₂ demonstrates no significant H₂ consumption, which means the neglectable reducibility of ZrO₂. Interestingly, for 75In₂O₃-25ZrO₂, the reduction signals of surface and the bulk In₂O₃ are located at a higher temperature than that of pure In₂O₃ catalyst, hinting a stronger interaction between In₂O₃ and ZrO₂.²⁹ This also shows the increasing O_v content over 75In₂O₃-25ZrO₂ catalyst, which is in accordance with the XPS result and the prominent catalytic activity.⁴²

CO₂ temperature programmed desorption (CO₂-TPD) was conducted to further investigate the CO₂ adsorption behaviour on the In₂O₃-ZrO₂ catalyst, as shown in Fig. S7b.† The profiles exhibit several significant CO₂ evolution signals from the ZrO₂ and 75In₂O₃-25ZrO₂ catalyst in the temperature range of 134–220, 273–315 and 396–477 °C. While the signal of CO₂ adsorbed on pure In₂O₃ are not detectable. The signal peak around 153 °C belongs to the physisorption of CO₂. Other signal peaks belong to the chemically absorbed CO₂ on the H₂-induced oxygen vacancy sites (O_v).⁴² Additionally, CO₂-TPD has been widely used to measure the surface basicity of catalysts, and high desorption temperature promised a strong basic site.⁴³ Compared with ZrO₂ catalyst, the CO₂ desorption peak of 75In₂O₃-25ZrO₂ catalyst shift to the higher temperatures of 315 °C and 75In₂O₃-25ZrO₂ catalyst have strong site at around 450 °C. Specifically, the addition of In enhances the strength of CO₂ adsorption on these sites, owing to the increase in basic intensity.⁴² The characterization results of H₂-TPR and CO₂-TPD consistently confirm that In₂O₃-ZrO₂ interface benefits the formation of oxygen vacancies, thus enhancing the ability of 75In₂O₃-25ZrO₂ catalyst to CO₂ adsorption and H₂ activation.

3.2. Catalytic performance

CO₂ hydrogenation mainly involves the following three reactions (5)–(7) to produce three products of CO, CH₄ and CH₃OH, respectively.

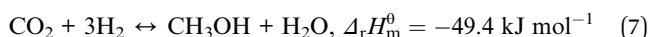
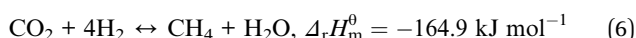
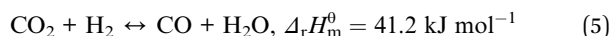


Fig. 2a shows the CO₂ conversion, CO selectivity, and CO yield over the five catalysts. The catalytic performance of pure ZrO₂ (*i.e.*, 0In₂O₃-100ZrO₂) is extremely poor, with CO₂ conversion of only 4% and CO selectivity of only 53%, while the

pure In₂O₃ (*i.e.*, 100In₂O₃-0ZrO₂) gives higher CO₂ conversion of 23.5% and CO selectivity of 95.8%. Interestingly, the In₂O₃-ZrO₂ catalysts (*i.e.*, 25In₂O₃-75ZrO₂, 50In₂O₃-50ZrO₂, and 75In₂O₃-25ZrO₂) all offers CO selectivity above 92%, with volcano evolution of CO₂ conversion. Most notably, the 75In₂O₃-25ZrO₂ offers the highest CO selectivity of 96% and highest CO₂ conversion of 28%. Due to a pronounced synergistic effect between ZrO₂ and In₂O₃, the In-Zr interface within the bimetallic oxides augments the density of O_v on the In₂O₃ surface, thereby significantly enhancing the adsorption and hydrogenation capacities towards CO₂. In addition, no methane can be detected, and a small amount of methanol was the only by-product.

The influence of reaction temperature, pressure, and gas hourly space velocity (GHSV) on catalytic performance is exhibited in Fig. 2b, c and S8.† At 0.1 MPa, and GHSV of 10 000 mL g⁻¹ h⁻¹, with the temperature rising from 300 to 500 °C, CO₂ conversion increases from 4% to 44%, and the highest CO selectivity is 96% at 400 °C. At 400 °C, and GHSV of 10 000 mL g⁻¹ h⁻¹, with the pressure increasing from 0.1 to 4 MPa, CO₂ conversion slightly increases from 28% to 29%, but CO selectivity decreases from 96% to 85% (with the formation of new by-product CH₄), because high reaction pressure is beneficial to CO₂ methanation reaction.⁴⁴ Moreover, at 0.1 MPa, and 400 °C, CO₂ conversion decreases from 35% to 27.7% with increasing GHSV from 6000 to 14 000 mL g⁻¹ h⁻¹, while the maximum CO selectivity is 94% at the GHSV of 10 000 mL g⁻¹ h⁻¹. Hence, the optimized reaction condition is as follows: 0.1 MPa, 400 °C and GHSV of 10 000 mL g⁻¹ h⁻¹. For the best catalyst 75In₂O₃-25ZrO₂, under the best reaction conditions, the CO₂ conversion and CO selectivity are 28% and 96% in the 200 h-test. However, for In₂O₃, the conversion decreases from 26% to 21%. Compared with pure In₂O₃, the stability of mixed oxides is obviously enhanced. Hence, the In₂O₃-ZrO₂ interface is of great importance in improving and maintaining catalytic activity (Fig. 2d). We compared the catalyst 75In₂O₃-25ZrO₂ with other catalysts including non-noble metal and noble metal catalysts in the RWGS reaction in Table S3.† CO₂ conversion, CO selectivity and STY of 75In₂O₃-25ZrO₂ are very promising. Notably, the STY of 75In₂O₃-25ZrO₂ is higher than other catalysts (apart from Ag/Al₂O₃). Furthermore, compared with noble metal catalysts, In-based catalysts have lower cost and more prospects in industry applications.

3.3. Surface intermediates and reaction mechanism

In situ FTIR was used to investigate the evolution of key surface intermediates for RWGS reaction, and the wavenumbers of the intermediates are summarized in Table S4.†^{33,34,36,37,39,45-55} Firstly, the three catalysts (75In₂O₃-25ZrO₂, In₂O₃, and ZrO₂) were placed into the chamber and reduced with hydrogen at 400 °C. Subsequently, CO₂ was introduced into the chamber for adsorption. Finally, the gaseous CO₂ was purged by He flow and the spectra were collected from 50 to 400 °C (Fig. 3). For 75In₂O₃-25ZrO₂ (Fig. 3a), the following characteristic bands can be observed: bi-HCOO* (bidentate formate, at 1350, 1589, 2873 and 2967 cm⁻¹);^{33,36,39,46,48,50,52-55} b-*OCH₃ (bridged methoxy, at



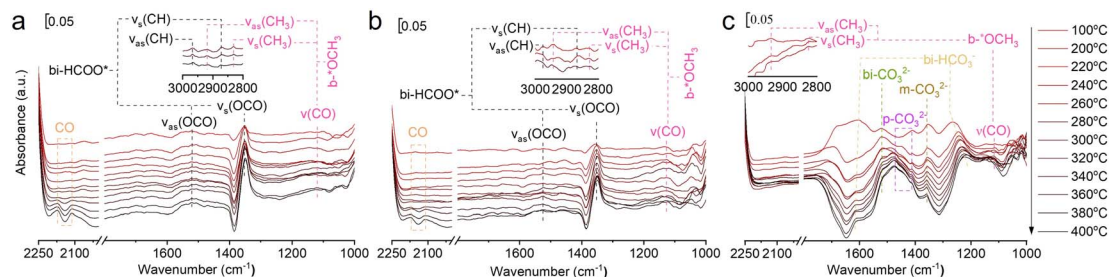


Fig. 4 *In situ* FTIR spectra of the reaction of CO₂ and H₂ over (a) 75In₂O₃-25ZrO₂, (b) In₂O₃, and (c) ZrO₂.

FTIR (Fig. 4). For 75In₂O₃-25ZrO₂, the characteristic band of CO is observed at 320 °C ($\nu(\text{CO}) = 2111.1$ and 2170 cm^{-1}). However, for In₂O₃, CO starts to appear at 360 °C, corresponding well with its lower catalytic activity. For ZrO₂, the characteristic bands of CO are not observed, showing that bi-HCO₃⁻, bi-CO₃²⁻, m-CO₃²⁻, and p-CO₃²⁻ can't be hydrogenated easily.⁴⁸ Lastly, for all the three catalysts, b-OCH₃^{*} is also observed, but this species could only be hydrogenated to CH₄ at relative higher 0.5 MPa, thus excluding the role of OCH₃^{*} playing under the reaction conditions (Fig. S9†). But the CH₄ is not formed in the real fixed-bed reaction process, which is likely caused by the different conditions between *in situ* FTIR and real reaction process.

Combined with the above analyses, it can be suggested that CO₂ hydrogenation on the In₂O₃-ZrO₂ catalyst through HCOO^{*} intermediates (Scheme S1†). H₂ adsorbed on the exposed surface of In₂O₃ crystal to form H₂^{*}, and then formed H_{in}^{*} and H_O^{*} at In site and O site, respectively. At the same time, CO₂ is adsorbed on a base on the surface of the composite oxide, activated by oxygen vacancy, and then combined with activated H_{in}^{*} to form formate intermediate (HCOO^{*}). HCOO^{*} interacts with the site of ZrO₂, undergoes the cleavage of C-O and C-H bonds, and forms O-H bonds at the same time, producing CO^{*} and OH^{*}, and CO^{*} desorbs to produce CO.^{33,37} In this case, ZrO₂ can not only modify In₂O₃, but also serve as an active site. In₂O₃-ZrO₂ constitutes a bimetallic In-Zr oxide catalyst system.

4. Conclusions

In this work, the optimal 75In₂O₃-25ZrO₂ and the contrastive In₂O₃, ZrO₂ were prepared by the coprecipitation method, and 75In₂O₃-25ZrO₂ exhibits excellent 28% conversion and 96% selectivity in the RWGS reaction under the best reaction conditions (400 °C, 0.1 MPa, H₂ : CO₂ molar ratio of 3 : 1 and gas hourly space velocity of $10\,000 \text{ mL g}^{-1} \text{ h}^{-1}$). XRD and STEM-EDX show that the In₂O₃-ZrO₂ solid solution is formed, and XPS testifies that the electron transfer effect plays an important role in this reaction. *In situ* FTIR shows that: for 75In₂O₃-25ZrO₂ with abundant In₂O₃-ZrO₂ interface, HCOO^{*} is easily hydrogenated into CO; however, for In₂O₃, the content of HCOO^{*} is relatively lower, thus contributing to its lower catalytic activity; for ZrO₂, the CO₃²⁻ is relatively stable, correlating well with its low catalytic activity. This work definitely testifies the pivotal role of HCOO^{*} in the RWGS reaction, but also paves a way to design bimetal oxide catalyst with excellent catalytic performance for RWGS reaction.

Conflicts of interest

The authors declare that there is no conflict of interest.

References

- S. J. Davis, K. Caldeira and H. D. Matthews, *Science*, 2010, **329**, 1330–1333.
- Z. Zhang, S.-Y. Pan, H. Li, J. Cai, A. G. Olabi, E. J. Anthony and V. Manovic, *Renewable Sustainable Energy Rev.*, 2020, **125**, 109799.
- A. Al-Mamoori, A. Krishnamurthy, A. A. Rownaghi and F. Rezaei, *Energy Technol.*, 2017, **5**, 834–849.
- A. Kaetelhoe, R. Meys, S. Deutz, S. Suh and A. Bardow, *Proc. Natl. Acad. Sci. U. S. A.*, 2019, **116**, 11187–11194.
- I. Mohsin, T. A. Al-Attas, K. Z. Sumon, J. Bergerson, S. McCoy and M. G. Kibria, *Cell Rep. Phys. Sci.*, 2020, **1**, 100104.
- L. J. Mueller, A. Kaetelhoe, M. Bachmann, A. Zimmermann, A. Sternberg and A. Bardow, *Front. Energy Res.*, 2020, **8**, 15.
- E. Kawai, A. Ozawa and B. D. Leibowicz, *Appl. Energy*, 2022, **328**, 120183.
- T. Len and R. Luque, *Green Chem.*, 2023, **25**, 490–521.
- Y. H. Zheng, M. Ma and H. Y. Shao, *Carbon Neutrality*, 2023, **2**, 23.
- O. S. Joo, K. D. Jung, I. Moon, A. Y. Rozovskii, G. I. Lin, S. H. Han and S. J. Uhm, *Ind. Eng. Chem. Res.*, 1999, **38**, 1808–1812.
- S. W. Park, O. S. Joo, K. D. Jung, H. Kim and S. H. Han, *Appl. Catal., A*, 2001, **211**, 81–90.
- R. Liu, D. Leshchev, E. Stavitski, M. Juneau, J. N. Agwara and M. D. Porosoff, *Appl. Catal., B*, 2021, **284**, 119787.
- D. Wang, Z. Xie, M. D. Porosoff and J. G. Chen, *Chem*, 2021, **7**, 2277–2311.
- A. D. N. Kamkeng and M. Wang, *Chem. Eng. J.*, 2023, **462**, 142048.
- Y. F. Zhu, B. Xie, R. Amal, E. C. Lovell and J. Scott, *Small Struct.*, 2023, **4**, 2200285.
- G. Kim, S. Shin, Y. Choi, J. Kim, G. Kim, K.-J. Kim and H. Lee, *JACS Au*, 2022, **2**, 1115–1122.
- R. Tang, Z. Zhu, C. Li, M. Xiao, Z. Wu, D. Zhang, C. Zhang, Y. Xiao, M. Chu, A. Genest, G. Rupprechter, L. Zhang, X. Zhang and L. He, *ACS Mater. Lett.*, 2021, **3**, 1652–1659.
- L. Chen, L. Kovarik and J. Szanyi, *ACS Catal.*, 2021, **11**, 12058–12067.



- 19 D. Zagoraios, S. Tsatsos, S. Kennou, C. G. Vayenas, G. Kyriakou and A. Katsaounis, *ACS Catal.*, 2020, **10**, 14916–14927.
- 20 L. Yang, L. Pastor-Perez, J. J. Villora-Pico, A. Sepulveda-Escribano, F. Tian, M. Zhu, Y.-F. Han and T. R. Reina, *ACS Sustain. Chem. Eng.*, 2021, **9**, 12155–12166.
- 21 Y. Meng, X. Y. Liu, Y. J. Ma, X. H. Gao and X. D. Wen, *Mol. Catal.*, 2022, **529**, 112538.
- 22 A. Pajares, X. Liu, J. R. Busacker, P. Ramirez de la Piscina and N. Homs, *Nanomaterials*, 2022, **12**, 3165.
- 23 J. J. Xu, X. X. Gong, R. R. Hu, Z. W. Liu and Z. T. Liu, *Mol. Catal.*, 2021, **516**, 111954.
- 24 G. Zhou and X. Ai, *Journal of Chongqing Technology and Business University*, 2023, **40**, 8–14.
- 25 Q. Sun, J. Ye, C.-j. Liu and Q. Ge, *Greenhouse Gases*, 2014, **4**, 140–144.
- 26 A. Tsoukalou, P. M. Abdala, D. Stoian, X. Huang, M.-G. Willinger, A. Fedorov and C. R. Mueller, *J. Am. Chem. Soc.*, 2019, **141**, 13497–13505.
- 27 L. Wang, Y. Dong, T. Yan, Z. Hu, A. A. Jelle, D. M. Meira, P. N. Duchesne, J. Y. Y. Loh, C. Qiu, E. E. Storey, Y. Xu, W. Sun, M. Ghossoub, N. P. Kherani, A. S. Helmy and G. A. Ozin, *Nat. Commun.*, 2020, **11**, 2432.
- 28 J. Wang, G. Zhang, J. Zhu, X. Zhang, F. Ding, A. Zhang, X. Guo and C. Song, *ACS Catal.*, 2021, **11**, 1406–1423.
- 29 T. P. Araujo, C. Mondelli, M. Agrachev, T. Zou, P. O. Willi, K. M. Engel, R. N. Grass, W. J. Stark, O. V. Safonova, G. Jeschke, S. Mitchell and J. Perez-Ramirez, *Nat. Commun.*, 2022, **13**, 5610.
- 30 P. C. Zonetti, V. L. Bridi, G. G. Gonzalez, C. R. Moreira, O. C. Alves, R. R. de Avellez and L. G. Appel, *ChemCatChem*, 2019, **11**, 4011–4020.
- 31 M. S. Frei, C. Mondelli, A. Cesarini, F. Krumeich, R. Hauert, J. A. Stewar, D. C. Ferre and J. Perez-Ramirez, *ACS Catal.*, 2020, **10**, 1133–1145.
- 32 X. Zhang, A. V. Kirilin, S. Rozeveld, J. H. Kang, G. Pollefeyt, D. F. Yancey, A. Chojecki, B. Vanchura and M. Blum, *ACS Catal.*, 2022, **12**, 3868–3880.
- 33 T.-y. Chen, C. Cao, T.-b. Chen, X. Ding, H. Huang, L. Shen, X. Cao, M. Zhu, J. Xu, J. Gao and Y.-F. Han, *ACS Catal.*, 2019, **9**, 8785–8797.
- 34 K. Pokrovski, K. T. Jung and A. T. Bell, *Langmuir*, 2001, **17**, 4297–4303.
- 35 H. Zhang, Y. Y. Dong, W. P. Fang and Y. X. Lian, *Chin. J. Catal.*, 2013, **34**, 330–335.
- 36 C. Yang, C. Pei, R. Luo, S. Liu, Y. Wang, Z. Wang, Z.-J. Zhao and J. Gong, *J. Am. Chem. Soc.*, 2020, **142**, 19523–19531.
- 37 C. Y. R. Vera, N. Manavi, Z. Zhou, L.-C. Wang, W. Diao, S. Karakalos, B. Liu, K. J. Stowers, M. Zhou, H. Luo and D. Ding, *Chem. Eng. J.*, 2021, **426**, 131767.
- 38 L. Yao, X. Shen, Y. Pan and Z. Peng, *J. Catal.*, 2019, **372**, 74–85.
- 39 Y. Wei, F. Liu, J. Ma, C. Yang, X. Wang and J. Cao, *Mol. Catal.*, 2022, **525**, 112354.
- 40 N. Siedl, P. Gügel and O. Diwald, *J. Phys. Chem.*, 2013, **117**, 20722–20729.
- 41 C. Gionco, M. C. Paganini, E. Giamello, R. Burgess, C. Di Valentin and G. Pacchioni, *Chem. Mater.*, 2013, **25**, 2243–2253.
- 42 Z. Lu, K. H. Sun, J. Wang, Z. T. Zhang and C. J. Liu, *Catalysts*, 2020, **10**, 1360.
- 43 Y. Cui, L. L. Xu, M. D. Chen, X. B. Lian, C. E. Wu, B. Yang, Z. C. Miao, F. G. Wang and X. Hu, *Catal. Sci. Technol.*, 2019, **9**, 5605–5625.
- 44 K. Stangeland, D. Kalai, H. L. Li and Z. X. Yu, *8th International Conference on Applied Energy (ICAE)*, 2016, vol. 105, pp. 2022–2027.
- 45 G. C. Cabilla, A. L. Bonivardi and M. A. Baltanás, *J. Catal.*, 2001, **201**, 213–220.
- 46 S. S. Dang, B. Qin, Y. Yang, H. Wang, J. Cai, Y. Han, S. G. Li, P. Gao and Y. H. Sun, *Sci. Adv.*, 2020, **6**, eaaz2060.
- 47 L. Z. Gao and C. T. Au, *J. Catal.*, 2000, **189**, 1–15.
- 48 L. Lin, S. Yao, Z. Liu, F. Zhang, N. Li, D. Vovchok, A. Martínez-Arias, R. Castañeda, J. Lin, S. D. Senanayake, D. Su, D. Ma and J. A. Rodriguez, *J. Phys. Chem. C*, 2018, **122**, 12934–12943.
- 49 Y. Wang, L. Zhu, Y. Liu, E. I. Vovk, J. Lang, Z. Zhou, P. Gao, S. Li and Y. Yang, *Appl. Surf. Sci.*, 2023, **631**, 157534.
- 50 S. Kattel, B. Yan, Y. Yang, J. G. Chen and P. Liu, *J. Am. Chem. Soc.*, 2016, **138**, 12440–12450.
- 51 B. Liu, T. Fang and Y. He, *Catal. Sci. Technol.*, 2022, **12**, 300–309.
- 52 W. Wang, Z. Qu, L. Song and Q. Fu, *J. Catal.*, 2020, **382**, 129–140.
- 53 W. Wang, Z. Qu, L. Song and Q. Fu, *J. Energy Chem.*, 2020, **40**, 22–30.
- 54 S. Collins, M. Baltanas and A. Bonivardi, *J. Catal.*, 2004, **226**, 410–421.
- 55 F. Ouyang, J. N. Kondo, K. Maruya and K. Domen, *Catal. Lett.*, 1998, **50**, 179–181.

